Nanoscale

PAPER

Microscopic mechanisms of vertical graphene and carbon nanotube cap nucleation from hydrocarbon growth precursors†

Cite this: *Nanoscale*, 2014, **6**, 9206

Umedjon Khalilov, Annemie Bogaerts and Erik C. Neyts*

Received 5th February 2014
Accepted 25th May 2014

DOI: 10.1039/c4nr00669k

www.rsc.org/nanoscale

Controlling and steering the growth of single walled carbon nanotubes is often believed to require controlling of the nucleation stage. Yet, little is known about the microscopic mechanisms governing the nucleation from hydrocarbon molecules. Specifically, we address here the dehydrogenation of hydrocarbon molecules and the formation of all-carbon graphitic islands on metallic nanoclusters from hydrocarbon molecules under conditions typical for carbon nanotube growth. Employing reactive molecular dynamics simulations, we demonstrate for the first time that the formation of a graphitic network occurs through the intermediate formation of vertically oriented, not fully dehydrogenated graphitic islands. Upon dehydrogenation of these vertical graphenes, the islands curve over the surface, thereby forming a carbon network covering the nanoparticle. The results indicate that controlling the extent of dehydrogenation offers an additional parameter to control the nucleation of carbon nanotubes.

Introduction

Carbon nanotubes in general and single walled carbon nanotubes in particular continue to attract widespread attention, thanks to their unique properties.[1] Especially the fact that the electronic properties can be tuned by changing fundamental CNT properties such as the diameter and chirality drives continued research on growth control, both experimentally and computationally.

The most often used experimental growth technique for CNTs is chemical vapor deposition, in which a hydrocarbon gas is catalytically dissociated at the surface of a suitable nanocatalyst particle at elevated temperature.[2] The elevated temperature in combination with the Gibbs–Thomson effect,[3,4] however, prevents the catalyst surface from maintaining a crystalline structure, thus making epitaxial growth impossible. Growth at lower temperature might be possible using plasma enhanced CVD, where the gas is activated in the plasma phase instead of on the catalyst surface.[5–8] If the growth temperature can be sufficiently lowered, epitaxial growth might be possible. The main obstacle at low temperature, however, is the cap formation and lift-off during the nucleation stage.[9]

In spite of a large number of studies dealing with this topic, the nucleation and growth of CNTs is still not fully understood. This is in part due to the difficulty in accessing the incubation and nucleation stage directly in the experiment. Complementary to experimental studies, atomic scale simulations are thus very useful to gain insight into the microscopic processes taking place. As a result, carbon nanotube growth has often been simulated, studying a variety of effects, including the (non)requirement of a temperature gradient,[10,11] the catalyst particle size,[12,13] the effect of applying an electric field,[14] the influence of ion bombardment,[15,16] the interaction strength between metal and carbon network,[9,17] the effect of the support–nanoparticle interaction strength,[18,19] the necessity of a carbide phase, both for Ni and Fe,[20–23] the effect of the carbon chemical potential,[24,25] and the importance of metal-mediated defect healing.[26,27] Recent reviews on modeling CNT growth can be found in ref. 7, 28 and 29.

One important assumption made in all of these simulations, however, is the use of pure carbon as the sole growth precursor, thus assuming instantaneous hydrocarbon decomposition on the catalyst surface. Hydrogen is thus never considered in any of these simulations. Balbuena *et al.* recently studied the influence of the growth precursor, using either C atoms or C_2 dimers as input gas.[30] These authors found that the C_2 precursor dissolves more slowly in the metal nanoparticle, and leads to less carbon association within the particle. Surface diffusion and nucleation from C_2 were found to be accelerated, increasing the risk of nanoparticle encapsulation. Also Shariat *et al.* employed two growth species, *viz.* thermalised C-atoms and energetic C-ions (modeled as fast neutrals), to mimic PECVD growth at low temperature.[16] These authors found that at 500 K, CNT-growth is promoted when the ion energy is in the order of 60 eV.

Shibuta *et al.* very recently performed *ab initio* molecular dynamics simulations to study the decomposition of methane on a Ni(111) surface for graphene growth,[31] which is closely

Department of Chemistry, Research Group PLASMANT, University of Antwerp, Universiteitsplein 1, 2610 Wilrijk, Antwerp, Belgium. E-mail: erik.neyts@uantwerpen.be

† Electronic supplementary information (ESI) available. See DOI: 10.1039/c4nr00669k

related to CNT growth.[28] These simulations demonstrated that CH_4 is stepwise decomposed into C and 4H, in agreement with classical MD simulations by Somers *et al.*[32] and Liu *et al.*[33] In this decomposition process, both CH_3 and CH are found as stable chemisorbed species on the nickel surface. The C atoms then diffuse into the subsurface region while the H atoms diffuse over the surface. Note, however, that in all of these simulations, the Ni surface was perfectly crystalline, without the curvature normally associated with nanocatalyst particles used for CNT growth.

Until now, there have been no reports on the atomistic mechanisms during nucleation of a cap or the growth of a CNT from a hydrocarbon source gas. In this work, we present the simulated formation of a graphitic network on Ni-nanocatalyst particles from acetylene (C_2H_2) and benzene (C_6H_6), two hydrocarbon gases which are known experimentally to yield CNTs.[34]

Computational details

Our simulations are based on combined molecular dynamics (MD) and time-stamped force-bias Monte Carlo (tfMC) simulations,[35] which were previously demonstrated to yield CNTs with definable chiralities.[27,36] In these simulations, energies and forces are derived from the ReaxFF interatomic potential,[37] using parameters developed by Mueller *et al.*[38] Previously, we had demonstrated that this force field faithfully reproduced various key properties of the Ni/C system, relevant for Ni-based CNT growth, including the C–C clustering energy, the C heat of solution in Ni and the formation volume of a C interstitial in bulk Ni.[27] This force field also produces binding energies of hydrogen and a wide variety of hydrocarbons on nickel in close agreement with quantum chemical calculations.[38] Moreover, of particular importance for the current work is the excellent agreement found between this force field and quantum chemical calculations found for dehydrogenation barriers on nickel.[38]

In our simulations, growth is accomplished by allowing hydrocarbon molecules (C_2H_2 or C_6H_6) to impinge on a Ni_{55} nanocluster. At any moment in time, the total number of gas phase molecules is kept constant. Thus, when a molecule impinges on and sticks to the nanocluster, a new molecule is introduced in the simulation box. When a hydrocarbon molecule adsorbs on the Ni cluster, the resulting structure is allowed to relax by application of tfMC.[35] During this relaxation stage, no new molecules are allowed to impinge on the cluster.

The pressure of the system is related to the impingement rate that we target in our simulations. In the ideal gas approximation, the impingement flux can be calculated as

$$J\left(\text{molecules per m}^2\text{ per s}\right) = \frac{N_A p}{\sqrt{2\pi MRT}}$$

where N_A is Avogadro's number, p is the pressure (in Pa), M is the molar mass (in kg per mole), R is the universal gas constant and T is the temperature (in K). The impingement fluxes simulated in this work are 0.02 nm^{-2} ns^{-1}, 0.1 nm^{-2} ns^{-1}, 0.2 nm^{-2} ns^{-1}, 1.0 nm^{-2} ns^{-1} and 2.0 nm^{-2} ns^{-1}, corresponding to a minimal pressure of 1.46 kPa (for acetylene at 1600 K and an impingement flux of 0.02 nm^{-2} ns^{-1}) and a maximal pressure of 270 kPa (for benzene at 1600 K and an impingement flux of 2 nm^{-2} ns^{-1}). For the highest impingement flux (2 molecules per nm^2 per ns), simulations were also carried out at 1000 K and 1400 K. For all other fluxes, the temperature was set to 1600 K, controlled by a canonical Bussi thermostat.[39] The average time between two impacts varies between 0.5 ns (for the highest impingement flux) and 50 ns (for the lowest impingement flux). The maximum total simulation time realized in these simulations was 2 μs.

The Ni cluster is either a gas phase cluster or a surface-bound cluster. In the case of a surface-bound cluster, the cluster is physisorbed on a virtual surface. This physisorption interaction is expressed by a one-dimensional averaged Lennard-Jones potential:[40]

$$F(z) = D_e\left\{\frac{1}{5}\left(\frac{\sigma}{z}\right)^{10} - \frac{1}{2}\left(\frac{\sigma}{z}\right)^{4}\right\}$$

where z is the atomic coordinate normal to the substrate. By choosing the D_e and σ parameters, a specific substrate can be mimicked. To study the influence of this substrate, we have chosen aluminum, in which the parameters are $D_e = 2.3$ eV and 0.03 eV, and $\sigma = 2.37$ Å and 2.976 Å for Ni–Al and C–Al pairs, respectively.[41]

For each distinct simulation condition (corresponding to a given combination of flux, temperature, and growth species, resulting in 36 different conditions), three to five independent simulations were carried out. The specific results described below correspond to a flux of 2 molecules per nm^2 per ns, unless specifically stated otherwise.

Results and discussion

1. Adsorption, desorption and pyrolysis

In Fig. 1, the typical C_2H_2 adsorption, dehydrogenation and subsequent H_2 desorption process at 1600 K is shown in a series of MD snapshots. The C_2H_2 molecule travels through the simulation box until it impinges on the Ni-cluster.

Upon impingement, the molecule adsorbs dissociatively with the formation of an acetylide C_2H radical and a H-atom. Also the second H-atom subsequently dissociates from the acetylide radical. The remaining C_2 dimer is found to diffuse back and forth into the first subsurface layer of the Ni cluster. Indeed, it was previously found from tight-binding simulations that C_2 dimers are stable in the Ni-subsurface region.[42] The H-atoms diffuse over the surface of the cluster, until they recombine and desorb as H_2. Employing nudged elastic band calculations,[43] we calculated the activation barrier for H-diffusion to be $E_a = 0.63$ eV, while the recombination activation energy is found to be $E_a = 1.63$ eV.[32] The H atoms may thus freely diffuse over the Ni surface until they either collide or recombine with another H atom and desorb as H_2.

In spite of the higher molecular adsorption rate of acetylene, the dehydrogenation mechanism is similar for C_2H_2 and C_6H_6. We found that upon adsorption, C_6H_6 either loses all of its

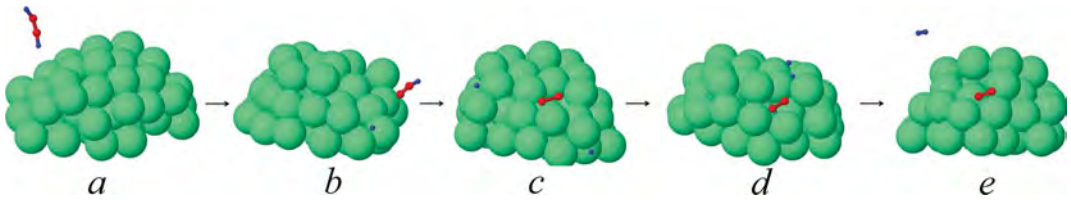

Fig. 1 Snapshots of structures observed during C_2H_2 decomposition on a surface-bound Ni cluster: (a) a C_2H_2 molecule moves randomly in a vacuum before interacting with the Ni cluster; (b) the molecule loses one of its hydrogen atoms upon impact on the cluster; both the C_2H radical and the H atom diffuse over the cluster surface; (c and d) dehydrogenation to a C_2 dimer; (e) finally, the hydrogen atoms recombine and desorb as H_2 molecules; C_2 diffuses into the cluster and eventually the C–C bond may be broken.

hydrogen atoms more or less simultaneously, leaving the carbon atoms connected as a hexagon or reconstructing them to a pentagon, or alternatively, all of its C–H as well as C–C bonds are gradually broken and its C atoms eventually dissolve into the cluster. Both mechanisms are illustrated in Fig. 2. Especially at a high impingement flux, the adsorbed benzene molecules do not dehydrogenate completely but rather form stable C_6H_4 or C_6H_3 rings standing vertically on the cluster surface. This is in agreement with simulations by Mueller who found that C_6H_3 converts to C_5H_3 and further decomposes by breaking either C–C or C–H bonds starting from a temperature of $T = 1750$ K.[44] A more detailed description of the dehydrogenation and graphitic network formation process is presented below.

Hydrogen atoms at the surface of the cluster may bind with a previously adsorbed and partially dehydrogenated hydrocarbon molecule, such as the C_2H (in the C_2H_2 case) or C_6H_3 (in the C_6H_6 case) radicals, as well as larger radicals, and then rehydrogenate the hydrocarbon.

An example of a rehydrogenation event is illustrated in Fig. 3 for a surface-bound C_5H_2 hydrocarbon chain during acetylene adsorption. Note that the appearance of such free-standing hydrocarbon chains may lead to the formation of carbon nanosheets.[45]

Impinging gas phase hydrocarbon species adsorb on the surface of the Ni cluster, as explained in the previous paragraphs, and subsequently dissociate and dissolve into the cluster where they preferentially occupy subsurface sites. Thus, at the beginning of the nucleation process, the number of adsorbed and dissolved carbon atoms rapidly rises as shown in Fig. 4a. The time shown corresponds to the sum of all

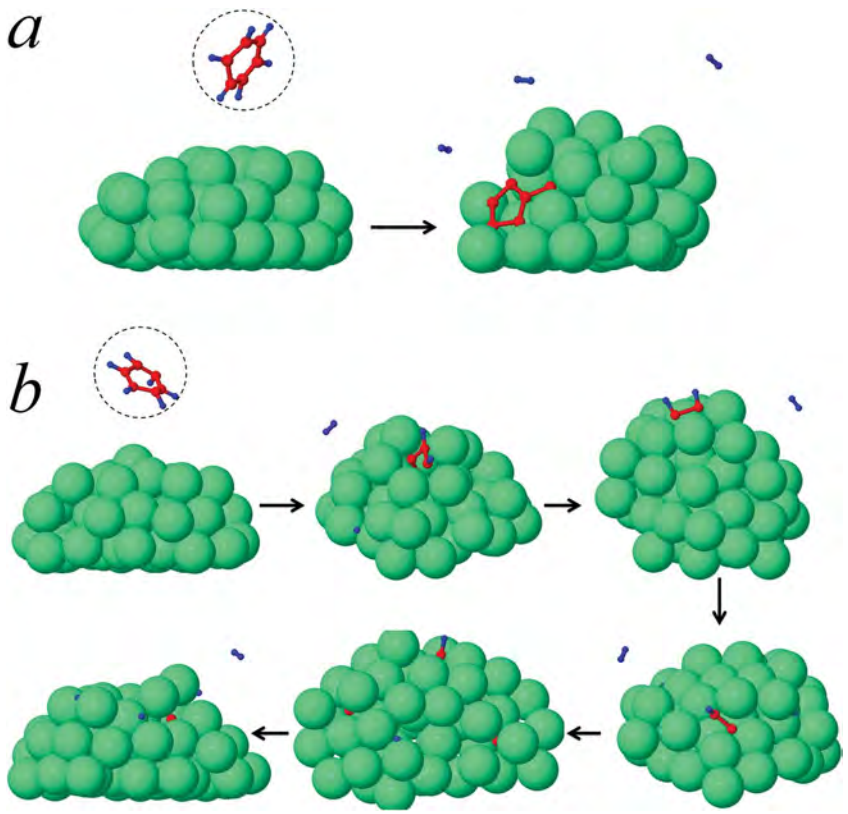

Fig. 2 Dehydrogenation processes for benzene: (a) complete dehydrogenation upon impact, with reorganization of the benzene ring into a pentagon; (b) gradual dehydrogenation and C–C bond cleavage, leading to dissolution of carbon in the cluster.

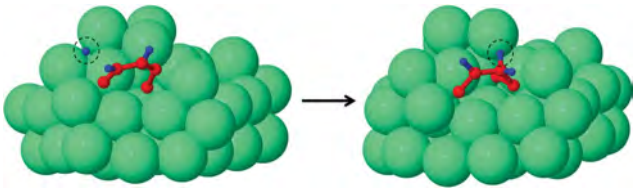

Fig. 3 Rehydrogenation of a previously adsorbed C_5H_2 hydrocarbon chain, slowing down the overall dehydrogenation rate. The H atom that is attached again to the C_5H_2 chain is indicated with a black dashed circle.

MD + tfMC cycles.[35] Note that surface-adsorbed C atoms still have bonds to H atoms, and must first lose all their hydrogen atoms in order to dissolve into the cluster. Subsequently, carbon atoms move into the bulk of the cluster, and then either quickly return to the surface or remain in the subsurface region. This process continues until there is no room left for additional carbon atoms to be added without forming C–C bonds at the surface or occasionally in the subsurface region. In the figure, therefore, the number of dissolved atoms remains constant (about 10) after saturation. The number of carbon atoms incorporated in the carbon network increases following the same trend as the total number of C atoms. The graph is similar for the C_6H_6 case.

In Fig. 4b, the evolution of the number of C-atoms and H-atoms in the structure is also shown as a function of simulation time for growth from C_2H_2 and growth from C_6H_6. The number of all C-atoms, *i.e.*, excluding vacuum atoms, is seen to continuously increase, both in the case of C_2H_2 and C_6H_6. Note that $N_C/2$ and $N_C/6$ are plotted for acetylene and benzene, respectively, to correlate with the number of incorporated/adsorbed/dissolved carbon atoms. It is clear that after the first 6 ns, the number of all C atoms is three times higher for acetylene than that for benzene, and so the adsorption rate of C_2H_2 is about three times higher than that of C_6H_6. However, the total number is nearly identical in both cases, as acetylene contains 2 and benzene contains 6 C-atoms. From this figure, it is also clear that the H-concentration stagnates to some constant value, and thus the net H-incorporation goes to zero after the initial start of the growth process, because of the desorption of H_2.

H_2 desorption from the cluster surface is essential for enabling the formation of a graphene network on the surface of the catalyst. It is found that hydrogen desorption (as H_2) does not require a critical minimum surface concentration of hydrogen atoms. Instead, H_2 desorption is found to occur as soon as the first hydrocarbon molecules adsorb on the surface, as shown in Fig. 5. Furthermore, it is clear from this figure that the H_2 desorption rate upon benzene and acetylene impact is similar, keeping in mind that benzene has three times more H atoms than acetylene.

It is known that hydrogen helps in the activation of the catalyst particles as well as enhances the yield of the growth. Furthermore, hydrogen diminishes the decomposition of the hydrocarbon feedstock and prevents excess carbon deposition at the surface of the catalyst particles. On the other hand, it may also hinder the formation of graphite-like carbon,[46,47] if its concentration is too high. Zhang *et al.*[47,48] and Behr *et al.*[49] also suggested that plasma including H atoms causes the breaking up of the sp^2 C–C bonds and the formation of sp^3 C–H bonds, resulting in etching of the carbon nanotubes.

Both C_6H_6 and C_2H_2 molecules are also found to dissociate in the gas phase at 1600 K, such that in this case also the

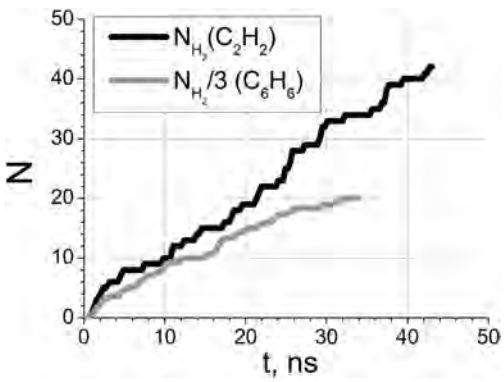

Fig. 5 Evolution of the number of desorbed H_2 molecules during the adsorption of either C_2H_2 or C_6H_6 molecules. Note that the number of desorbed H_2 molecules upon C_6H_6 impact is divided by three, to allow a better comparison with C_2H_2 impact.

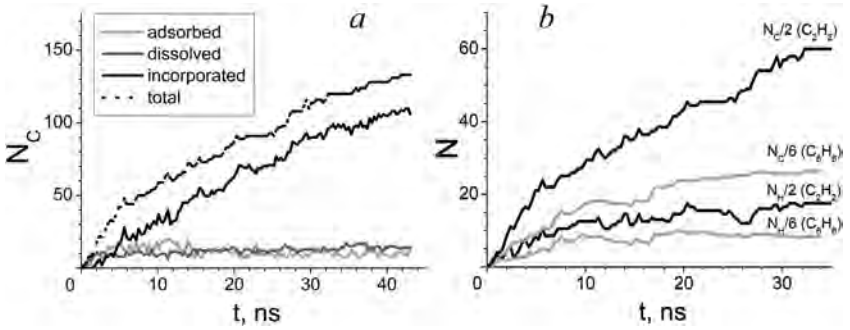

Fig. 4 (a) Evolution of the number of adsorbed, dissolved, incorporated and total carbon atoms in the case of acetylene impact; (b) evolution of the total number of carbon (N_C) and hydrogen (N_H) atoms in/on the Ni cluster during the nucleation process, upon impact of either acetylene or benzene molecules. The number of adsorbed C or H atoms upon C_2H_2 and C_6H_6 impact is divided by two and six, respectively, to allow a better comparison.

decomposition products may impinge on and bind with the nickel cluster. This gas phase pyrolysis is in agreement with experimental studies showing the formation of acetylene, ethylene, methane, carbon, as well as a variety of other species.[50–58] Thus, the gas phase also contains a fraction of C_xH_{x-y} species. Under high flux and high temperature conditions, we find that up to 50% of the benzene molecules are transformed into other species, most notably acetylene molecules.[57] In the case of acetylene, gas phase pyrolysis occurs for about 40% of the molecules. In this case, mostly C_2 dimers and acetylide C_2H radicals are found as pyrolysis products.[47,48] A detailed analysis of the pyrolysis mechanisms for both C_6H_6 and C_2H_2 is presented in Tables 1 and 2 in the ESI.† Note that in contrast to the experiments, polyaromatic rings are not formed in our simulations, as the pyrolysis products rapidly adsorb on the nickel cluster. Additionally, we find that at high temperature, molecules often lose a H-atom upon impingement, and the resulting C_xH_{x-1} radical is scattered from the surface into the gas phase. The H-atom may remain on the surface or also scatter into the gas phase. The resulting gas phase H-atoms may also recombine with the gas phase hydrocarbon radicals. Our calculations show also that the appearance of these gas phase decomposition products depends only slightly on the pressure. As we here focus on the formation of a graphitic network from either C_2H_2 or C_6H_6, we limit the influence of the gas phase pyrolysis products and hydrogen gas[46] and remove these products every 10^6 simulation steps.

2. *k*-Coefficient

As mentioned above, the crucial role of the catalytic hydrocarbon decomposition in catalyzed carbon nanotube growth will determine the adsorption/desorption rate of H atoms and whether or not tube growth may occur.[46–49] In other words, incorporation of carbon atoms in the carbon network on the catalyst is enhanced when hydrogen extensively desorbs from the surface. We thus introduce a coefficient k in order to assess the dehydrogenation degree of the source gas on the catalytic metal cluster as follows:

$$k = \frac{mN_C - nN_H}{mN_C + nN_H}$$

where N_C and N_H are the number of carbon and hydrogen atoms, respectively, in the cluster, and n and m are the number of carbon atoms and hydrogen atoms, respectively, in the impinging C_nH_m molecule/radical. The k-coefficient allows us to easily differentiate between physisorption of the hydrocarbon on the cluster surface without any subsequent hydrogen desorption ($k = 0$), complete dehydrogenation and subsequent desorption of H_2 ($k = 1$), and partial dehydrogenation and H_2-desorption ($0 < k < 1$).

In Fig. 6, a series of Ni/C structures is shown for various values of the k-coefficient. An increasing value for k indicates a lower H-concentration at the surface, and thus a higher probability for carbon cluster coalescence and eventually cap formation. Thus, $k = 1$ (*i.e.*, $N_H = 0$) is the ideal surface condition for nanotube growth. Note that this condition corresponds to all nanotube growth simulations reported in the literature so far.

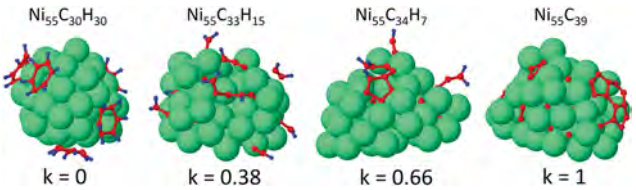

Fig. 6 $Ni_{55}C_yH_z$ structures corresponding to various k-coefficients, showing a gradual lower H-concentration for an increasing k value.

The k-coefficient depends on the growth temperature and the type of carbon precursor.

A comparison between acetylene and benzene at various temperatures is shown in Fig. 7, in terms of the k-coefficient as a function of the number of simulation steps. It can be seen that the k-coefficient, and thus the dehydrogenation efficiency, is somewhat higher for acetylene than for benzene at all temperatures investigated, as mentioned in the previous section. Furthermore, the dehydrogenation increases with temperature, which is attributed to an increasing probability of H-recombination at the surface. Indeed, the latter has a high activation barrier of 1.63 eV as mentioned above. In general, the H_2 desorption and thus the k-coefficient will also depend on the hydrocarbon flux (or feedstock pressure), the cluster size and the type of substrate which, however, we have not investigated here.

Also, we rely on the fact that the change in k is not directly indicative of how the decomposition has taken place, either by pyrolysis or catalysis. In the pyrolysis process, the precursor can lose some of its hydrogen atoms before it impinges on the catalyst particle. Hydrogen atoms in the gas phase, however, may in turn initiate another pyrolysis reaction or alternatively impinge on the catalyst surface. Consequently, both the decomposed molecule/radical and hydrogen atom eventually impinge on the cluster. In our simulations, all decomposed

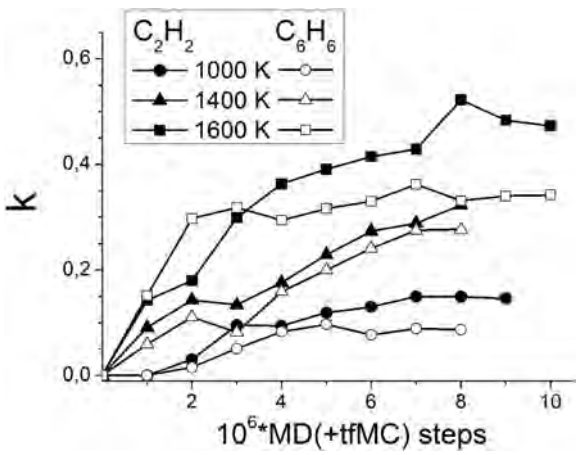

Fig. 7 Evolution of the k-coefficient during either C_2H_2 or C_6H_6 adsorption, for three different cluster temperatures, for a surface-bound Ni-cluster.

particles eventually chemisorb on the cluster. The hydrogen concentration at the surface (and thus the *k*-coefficient) is then determined by the subsequent desorption of H_2 molecules from the surface as well as the arrival rate of H atoms to the surface. Therefore, the *k*-coefficient does not depend on how the precursor decomposes.

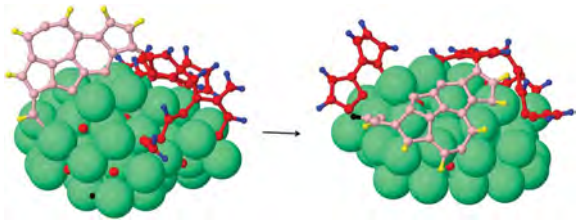

Fig. 9 Dehydrogenation of the vertically oriented graphene sheets, leading to the formation of horizontally oriented graphene patches curving over the surface. The pink atoms denote the carbon patch that is transformed from standing upright to horizontally curved over the surface, while the red atoms denote all other carbon atoms.

3. Evolution of the cap nucleation process

The typical evolution of the carbon network on the Ni-cluster is shown in Fig. 8, both for acetylene and benzene impact.

The molecules initially adsorb after impingement, after which one or several C–H bonds are typically broken as described above, resulting in chemisorption (Fig. 8a). The remaining radicals, however, are still very mobile, and can easily diffuse over the surface of the cluster. When C-atoms and C-dimers are formed through dehydrogenation and C–C bond cleavage, they can dissolve in and diffuse through the subsurface area of the cluster. Above the supersaturation limit, carbon also starts to segregate at the surface from the subsurface region, in accordance with the vapor–liquid–solid mechanism. In this stage, rings are easily formed on the surface (Fig. 8b). As these rings are also mobile on the surface, they may concatenate and form small graphitic islands. In contrast to growth from H-free precursors, however, these small islands, typically containing three or four rings, are not lying flat on the surface, but are standing upright, normal to the surface (Fig. 8c). Such growth behavior is similar to the formation of carbon nanosheets in the initial stage of nanowall growth.[45] However, these patches gradually lose their hydrogen atoms and curve over the surface to connect to each other (Fig. 8d). This transformation from vertically oriented patches to horizontally oriented patches is displayed in more detail in Fig. 9.

Note that this transformation is required for cap nucleation to occur. Indeed, eventually, this concatenation process leads to the formation of either a graphitic cap or the encapsulation of the cluster. Also, we found both horizontal- and vertical-oriented patches in the same structure for both C_2H_2 and C_6H_6 impacts, in agreement with experiments reported by Malesevic *et al.*[59] They synthesized CNTs together with carbon nanowalls (CNWs) in one single experiment on a Ni coated substrate using an acetylene precursor. Furthermore, in a few cases, we observe that the addition of new hydrocarbon molecules to the structure occurs much faster than the dehydrogenation, leading to the formation of a number of parallel vertically oriented graphene sheets or CNWs as mentioned before. An example of this is shown in Fig. 10. Note that these vertical sheets are almost defect-free and consist of almost only hexagons. The distance between the sheets is about 3.0 Å, which is in fairly good agreement with experimental observations (3.4 Å).[45,59] Although we obtained such atomically thin, free-standing carbon nanosheets or CNWs as observed in many experimental studies,[8] such nanosheets/nanowalls are experimentally mostly synthesized in a PECVD setup where electric fields are present. In contrast, our simulations were performed to mimic the CVD process and we thus assume that our vertical patches, which are not supported or stabilized by an electric field, will eventually curve over the surface as horizontal patches.

In the cap nucleation process, we can distinguish three stages, as shown in Fig. 11. In this figure, the evolution of the

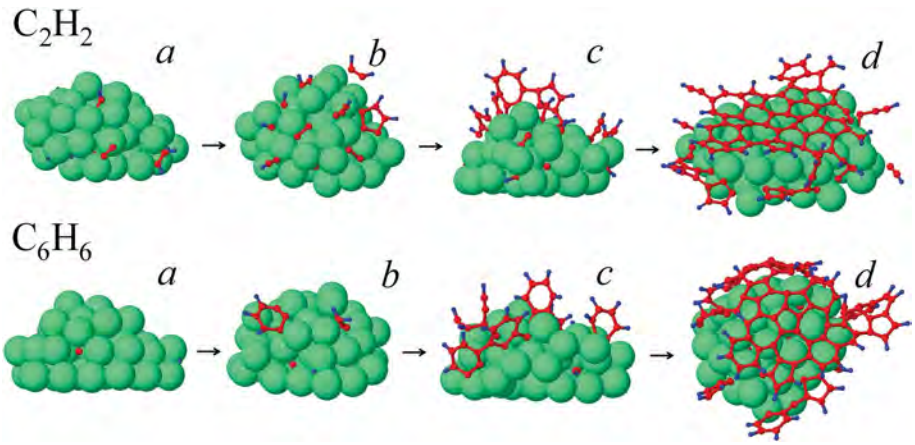

Fig. 8 Evolution of the graphitic network formation process upon impact of acetylene and benzene: (a) in the initial stage, almost all adsorbed C atoms diffuse into the Ni cluster; (b) after saturation, initial rings are formed on the cluster; (c) subsequently, hydrogenated graphitic patches arrange in a vertical orientation; (d) after dehydrogenation, the graphene-like sheets curve over the surface and connect to form an extensive graphitic network, forming either a CNT cap or leading to encapsulation of the cluster.

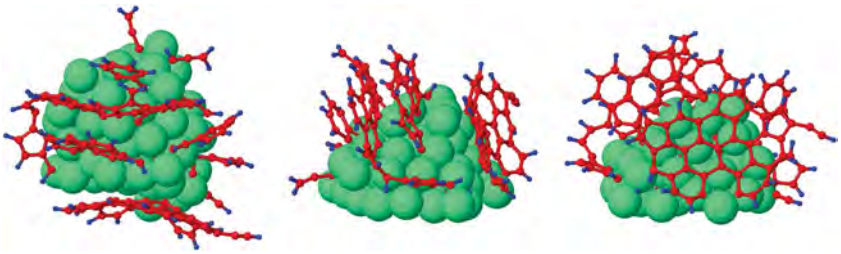

Fig. 10 Formation of vertically oriented graphene patches from top view (left), side view (middle) and front view (right). The figure shows that the patches are of high quality (*i.e.*, consisting of almost exclusively hexagons), and the edges are fully hydrogenated.

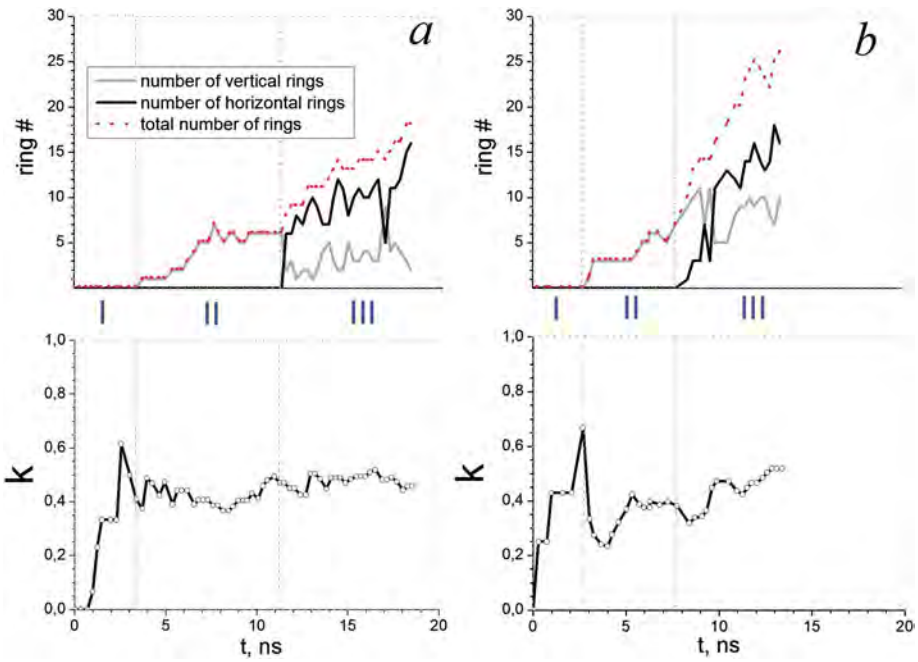

Fig. 11 Upper panel: number of rings (summed over pentagons, hexagons, and heptagons) as a function of time during the nucleation stage at an impingement flux of 2 nm^{-2} ns^{-1}, for acetylene (a) and benzene (b). The dotted red line is the total number of rings, the solid grey line is the number of vertical rings (*i.e.*, rings in vertically oriented patches), and the solid black line is the number of horizontal rings (*i.e.*, rings in patches curving over the surface). The three nucleation stages are denoted by roman numerals. The lower panel shows the evolution of the *k*-coefficient as a function of the simulated time.

number of graphitic rings (counted as the sum of all pentagons, hexagons and heptagons) as well as the *k*-coefficient is shown as a function of time. It can be seen that the *k*-coefficient converges rapidly to a value around 0.4, with a slightly higher value for acetylene than for benzene impact. We denote the initial stage as the time in which the value for *k* rises, after which it continues to increase slowly. The number of graphitic rings is still negligible in this stage. In the second stage, vertically oriented graphitic islands (denoted by "vertical rings") are formed, but no horizontal graphitic islands (denoted by "horizontal rings"), *i.e.*, no graphitic patches curving over the surface are formed yet. As mentioned above, the vertically oriented graphitic patches gradually lose hydrogen atoms at their edges, either by recombination of H-atoms in the vertical patch or by migration to the cluster and recombination on the cluster surface. This leads to a local increase in the *k*-coefficient, although the overall value of the *k*-coefficient stays more or less constant, and the patches start to curve over the surface. We denote the third stage when besides vertically oriented patches, horizontally oriented graphitic patches are also formed. Specifically, the onset of the third stage is characterized by transformation of vertically oriented patches to horizontally oriented patches.

From Fig. 11, it is clear that benzene shows a higher tendency towards the formation of vertical patches, even in the third stage (as the ratio of vertical rings to horizontal rings is higher in the case of benzene), indicative of the more difficult dehydrogenation of benzene compared to acetylene, as discussed above. This also corresponds to the somewhat higher *k*-coefficients observed for acetylene as compared to benzene, as shown above in Fig. 7b. Both in the case of acetylene and benzene, it is also clear that the number of vertically oriented rings (*i.e.*, rings pertaining to vertically oriented patches, normal to the surface) stagnates, while the number of rings

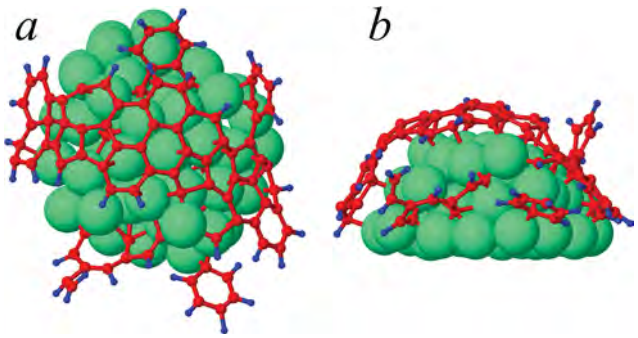

Fig. 12 Cap-like structure formed from benzene impact at 1600 K and 12.7 kPa in (a) top view and (b) side view.

parallel to the surface continues to increase. This is indeed a necessary condition for cap nucleation and lift-off. A cap-like structure, as formed in a growth simulation from benzene at 1600 K and at a pressure of 12.7 kPa, is illustrated in Fig. 12, both in the top view and the side view.

Conclusions

Nucleation and growth of graphitic networks on Ni-nanoclusters from hydrocarbon molecules was studied employing reactive molecular dynamics simulations. While the vapor–liquid–solid mechanism is still found to be responsible for the segregation of carbon at the surface and the formation of some rings, we observe that graphitic islands on the catalyst are typically not fully dehydrogenated at their edges, leading to their vertical orientation. These vertical graphenes gradually lose their hydrogen atoms, allowing them to curve over the surface, connect, and form a continuous graphitic network. This leads to either cap formation or encapsulation of the nanocatalyst. These simulations provide new insight into the nucleation of carbon nanotubes from hydrocarbon molecules.

Acknowledgements

This work was carried out in part using the Turing HPC infrastructure at the CalcUA core facility of the Universiteit Antwerpen (UA), a division of the Flemish Supercomputer Center VSC, funded by the Hercules Foundation, the Flemish Government (department EWI) and the UA.

References

1 M. Terrones, *Annu. Rev. Mater. Res.*, 2003, **33**, 419–501.
2 W.-H. Chiang and R. M. Sankaran, *Nat. Mater.*, 2009, **8**, 882–886.
3 Y. Shibuta and T. Suzuki, *Chem. Phys. Lett.*, 2010, **498**, 323–327.
4 K. Ostrikov and H. Mehdipour, *ACS Nano*, 2011, **5**, 8372–8382.
5 E. J. Bae, Y.-S. Min, D. Kang, J.-H. Ko and W. Park, *Chem. Mater.*, 2005, **17**, 5141–5145.
6 E. Mora, J. M. Pigos, F. Ding, B. I. Yakobson and A. R. Harutyunyan, *J. Am. Chem. Soc.*, 2008, **130**, 11840–11841.
7 E. C. Neyts, *J. Vac. Sci. Technol., B: Microelectron. Nanometer Struct.–Process., Meas., Phenom.*, 2012, **30**, 030803.
8 K. Ostrikov, E. C. Neyts and M. Meyyappan, *Adv. Phys.*, 2013, **62**, 113–224.
9 J. C. Burgos, H. Reyna, B. I. Yakobson and P. B. Balbuena, *J. Phys. Chem. C*, 2010, **114**, 6952–6958.
10 F. Ding, A. Rosén and K. Bolton, *Chem. Phys. Lett.*, 2004, **393**, 309–313.
11 F. Ding, A. Rosén and K. Bolton, *Carbon*, 2005, **43**, 2215–2217.
12 Y. Shibuta and S. Maruyama, *Chem. Phys. Lett.*, 2003, **382**, 381–386.
13 F. Ding, A. Rosén and K. Bolton, *Chem. Phys.*, 2004, **121**, 2775–2779.
14 E. C. Neyts, A. C. T. van Duin and A. Bogaerts, *J. Am. Chem. Soc.*, 2012, **134**, 1256–1260.
15 E. C. Neyts, K. Ostrikov, Z. J. Han, S. Kumar, A. C. T. van Duin and A. Bogaerts, *Phys. Rev. Lett.*, 2013, **110**, 065501.
16 M. Shariat, S. I. Hosseini, B. Shokri and E. C. Neyts, *Carbon*, 2013, **65**, 269–276.
17 M. A. Ribas, F. Ding, P. B. Balbuena and B. I. Yakobson, *J. Chem. Phys.*, 2009, **131**, 224501.
18 D. A. Gomez-Gualdron, G. D. McKenzie, J. F. J. Alvarado and P. B. Balbuena, *ACS Nano*, 2012, **6**, 720–735.
19 Y. Shibuta and J. A. Elliott, *Chem. Phys. Lett.*, 2006, **427**, 365–370.
20 D. A. Gomez-Gualdron and P. B. Balbuena, *Carbon*, 2013, **57**, 298–309.
21 Y. Ohta, Y. Okamoto, S. Irle and K. Morokuma, *ACS Nano*, 2008, **2**, 1437–1444.
22 A. J. Page, H. Yamane, Y. Ohta, S. Irle and K. Morokuma, *J. Am. Chem. Soc.*, 2010, **132**, 15699–15707.
23 A. Börjesson and K. Bolton, *J. Phys. Chem. C*, 2010, **114**, 18045–18050.
24 H. Amara, J.-M. Roussel, C. Bichara, J.-P. Gaspard and F. Ducastelle, *Phys. Rev. B: Condens. Matter Mater. Phys.*, 2009, **79**, 014109.
25 H. Amara, C. Bichara and F. Ducastelle, *Phys. Rev. Lett.*, 2008, **100**, 056105.
26 M. Diarra, H. Amara, C. Bichara and F. Ducastelle, *Phys. Rev. B: Condens. Matter Mater. Phys.*, 2012, **85**, 245446.
27 E. C. Neyts, A. C. T. van Duin and A. Bogaerts, *J. Am. Chem. Soc.*, 2011, **133**, 17225–17231.
28 J. A. Elliott, Y. Shibuta, H. Amara, C. Bichara and E. C. Neyts, *Nanoscale*, 2013, **5**, 6662–6676.
29 Y. Shibuta, *Diamond Relat. Mater.*, 2011, **20**, 334–338.
30 D. A. Gomez-Gualdron, J. M. Beetge, J. C. Burgos and P. B. Balbuena, *J. Phys. Chem. C*, 2013, **117**, 10397–10409.
31 Y. Shibuta, R. Arifin, K. Shimamura, T. Oguri, F. Shimojo and S. Yamaguchi, *Chem. Phys. Lett.*, 2013, **565**, 92–97.
32 W. Somers, A. Bogaerts, A. C. T. van Duin, S. Huygh, K. M. Bal and E. C. Neyts, *Catal. Today*, 2013, **211**, 131–136.
33 B. Liu, M. T. Lusk and J. F. Ely, *Surf. Sci.*, 2012, **606**, 615–623.
34 C. P. Deck and K. Vecchio, *Carbon*, 2006, **44**, 267–275.

35 M. J. Mees, G. Pourtois, E. C. Neyts, B. J. Thijsse and A. Stesmans, *Phys. Rev. B: Condens. Matter Mater. Phys.*, 2012, **85**, 134301.
36 E. C. Neyts, Y. Shibuta, A. C. T. van Duin and A. Bogaerts, *ACS Nano*, 2010, **11**, 6665–6672.
37 A. C. T. van Duin, S. Dasgupta, F. Lorant and W. A. Goddard III, *J. Phys. Chem. A*, 2001, **105**, 9396–9409.
38 J. E. Mueller, A. C. T. van Duin and W. A. Goddard III, *J. Phys. Chem. C*, 2010, **114**, 4939–4949.
39 G. Bussi, D. Donadio and M. Parrinello, *J. Chem. Phys.*, 2007, **126**, 014101.
40 S. Maruyama, T. Kurashige, S. Matsumoto, Y. Yamaguchi and T. Kimura, *Microscale Thermophys. Eng.*, 1998, **2**, 49–62.
41 T. R. Cundari, S. S. Janardan, O. Olatunji-Ojo and B. R. Wilson, *Int. J. Quantum Chem.*, 2011, **111**, 4303–4308.
42 M. Moors, H. Amara, T. V. de Bocarmé, C. Bichara, F. Ducastelle, N. Kruse and J.-C. Charlier, *ACS Nano*, 2010, **3**, 511–516.
43 G. Henkelman, B. P. Uberuage and H. Jonsson, *J. Chem. Phys.*, 2000, **113**, 9901.
44 J. E. Mueller, A. C. T. van Duin and W. A. Goddard III, *J. Phys. Chem. C*, 2010, **114**, 5675–5685.
45 M. Zhu, J. Wang, B. C. Holloway, R. A. Outlaw, X. Zhao, K. Hou, V. Shutthanandan and D. Manos, *Carbon*, 2007, **45**, 2229–2234.
46 F. Ohashi, G. Y. Chen, V. Stolojan and S. R. P. Silva, *Nanotechnology*, 2008, **19**, 445605.
47 G. Zhang, P. Qi, X. Wang, Y. Lu, X. Li, R. Tu, S. Bangsaruntip, D. Mann, L. Zhang and H. Dai, *Science*, 2006, **314**, 974–977.
48 G. Zhang, P. Qi, X. Wang, Y. Lu, D. Mann, X. Lu and H. Dai, *J. Am. Chem. Soc.*, 2006, **128**, 6026–6027.
49 M. J. Behr, E. A. Gaulding, K. A. Mkhoyan and E. S. Aydil, *J. Vac. Sci. Technol., B: Microelectron. Nanometer Struct.–Process., Meas., Phenom.*, 2010, **28**, 1187–1194.
50 C. T. Brooks, S. Peacock and B. G. Reuben, *J. Chem. Soc., Faraday Trans.*, 1979, **75**, 652–662.
51 M. H. Back, *Can. J. Chem.*, 1971, **49**, 2199–2204.
52 K. M. Ervin, S. Groner, S. E. Barlow, M. K. Gilles, A. G. Harrison, V. M. Bierbaum, C. H. DePuy, W. C. Lineberger and G. B. Ellison, *J. Am. Chem. Soc.*, 1990, **112**, 5750–5759.
53 F. Stahl, P. V. R. Schleyer, H. F. Schaefer III and R. I. Kaiser, *Planet. Space Sci.*, 2002, **50**, 685–692.
54 M. B. Colket, *Prepr. Pap. – Am. Chem. Soc., Div. Fuel Chem.*, 1986, **31**, 98–107.
55 R. S. Slysh and C. R. Kinney, *J. Phys. Chem.*, 1965, **65**, 1044–1045.
56 W. Eisfeld, *Phys. Chem. Chem. Phys.*, 2005, **7**, 3924–3932.
57 F. Cataldo, *Ultrason. Sonochem.*, 2000, **7**, 35–43.
58 T. Tanzawa, Jr and W. C. Gardiner, *J. Phys. Chem.*, 1980, **84**, 236–239.
59 A. Malesevic, S. Vizireanu, R. Kemps, A. Vanhulsel, C. Van Haesendonck and G. Dinescu, *Carbon*, 2007, **45**, 2932–2937.